DOI: 10.1021/cg900981q

CRYSTAL GROWTH & DESIGN Article

2010, Vol. 10
587–596

# Synthesis Mechanisms of Organized Gold Nanoparticles: Influence of Annealing Temperature and Atmosphere

Mikhael Bechelany,*,† Xavier Maeder,† Jessica Riesterer,† Jihane Hankache,† Damiana Lerose,‡ Silke Christiansen,‡ Johann Michler,† and Laetitia Philippe†

†*EMPA, Swiss Federal Laboratories for Materials Testing and Research, Laboratory for Mechanics of Materials and Nanostructures, Feuerwerkerstrasse 39, CH-3602 Thun, Switzerland and* ‡*Institut für Photonische Technologien, Albert-Einstein-Strasse 9, D-07745 Jena, Germany, and Max-Planck Institute for Microstructure Physics, Weinberg 2, D-06120 Halle, Germany*

*Received August 18, 2009; Revised Manuscript Received November 25, 2009*

**ABSTRACT:** We report on the synthesis of organized arrays of gold (Au) nanoparticles on thermally oxidized Si wafers using sputtering as a metal deposition method in combination with sphere lithography. This simple process leads to the formation of a honeycomb mask of Au at room temperature (RT). We study the transformation mechanism of this honeycomb mask to a hexagonal array of Au nanoparticles by annealing at different temperatures and in different atmospheres. The underlying mechanisms of pattern formation during annealing are coalescence of particles and Ostwald ripening and depend on temperature and atmosphere. The crystallinity and orientation of the nanoparticles with respect to the underlying substrate is analyzed by electron backscatter diffraction (EBSD), and the control of the morphology, size, shape, and orientation in different atmospheres (argon (Ar), nitrogen ($N_2$), air, hydrogen ($H_2$), and vacuum) is discussed.

## Introduction

Metal nanoparticle (NP) arrays have been a subject of great interest due to their differing physical properties compared with their bulk counterparts.[1] These NPs have found potential applications for magnetic data storage,[2,3] chemical catalysis,[4] optoelectronic devices,[5] biosensors,[6,7] and catalysts for the growth of aligned one-dimensional nanostructures.[8,9] In the past few years, the formation of regular patterns of dots on a surface has been achieved by different methods, such as focused ion beam (FIB) or electron-beam lithography,[10,11] molecular beam epitaxy (MBE),[12] chemical-vapor deposition (CVD),[13] or self-assembly[14,15] and template-based methods using porous anodic alumina (PAA) membranes as evaporation masks.[16] These methods offer excellent control over the particle size, shape, and spacing but are not satisfactory due to drawbacks such as low throughput, slow deposition speed, and high production cost.

As an alternative to these methods, natural lithography using two-dimensional (2D) colloidal crystals has been proposed by Deckman and Dunsmuir and has attracted attention due to the simplicity of the process.[17] In recent years, various techniques, often called "colloidal lithography" or "nanosphere lithography" (NSL), have been described for the nano/microfabrication or nano/micropatterning of a wide variety of semiconductor,[18] ceramic,[19] and metal[20,21] substrates, and to study the variation of the morphology of these nanoparticles by annealing.[22] In 1999, Burmeister et al.[23] studied the morphology variation of an array of triangular gold (Au) particles deposited by evaporation in high vacuum followed by thermal annealing. Sun et al.[24] studied the variation in morphology of triangular Au particles while heating with a laser. Tan et al.[25] used the electron-beam evaporation of Au with NSL for the synthesis of similar triangular Au arrays. They studied the influence of different experimental parameters (thermal annealing, thickness of Au, etc.) on the alignment, size, and shape of these nanoparticles. Müller et al.[26] studied the formation of faceted Au nanodots arranged in periodic arrays and explored the dewetting behavior in air. All of these methods use costly thermal or electron-beam evaporators in high vacuum, sometimes combined with reactive-ion etching in order to form triangular Au NPs at room temperature (RT). The variation in the morphology, crystallinity, and the mechanism of pattern formation of organized Au NPs as a function of annealing temperature and atmosphere has yet to be addressed.

Recently, we reported two types of site-selective metal deposition methods based on colloidal crystal templating for the synthesis of Au NPs.[27] The controllability of the morphology and crystallinity of these Au NPs depends on the choice of processing method. In this paper, we describe the fabrication of ordered hexagonal arrays of Au NPs using sputtering as a metal deposition method and patterned using NSL. This easy deposition process (deposition of Au in low vacuum, ~1 Pa, at RT) results in a honeycomb mask of Au. For the first time, the transformation mechanism of this honeycomb mask to a hexagonal array of Au NPs by thermal annealing at different temperatures and in different atmospheres has been studied. This morphology of Au allows the study of mechanisms of the self-organization of the NPs.[4] We will show that the mechanisms can range from coalescence to Ostwald ripening depending on temperature and atmospheres.

Due to the substantial influence of temperature, annealing atmospheres, and Au surface states on diffusion and mobility of Au on silicon (Si) substrates, the controllability of the organization, morphology, and crystallinity of these NPs in different atmospheres (Ar, $N_2$, air, $H_2$, and vacuum) and annealing temperatures was studied. The orientation of the NPs with substantial statistics was carried out using electron backscatter diffraction (EBSD). To the best of our knowledge, this is the first time that the transformation of a

*To whom correspondence should be addressed. Phone: +41332283627. Fax: +41332284490. E-mail: mikhael.bechelany@empa.ch.



Published on Web 01/07/2010

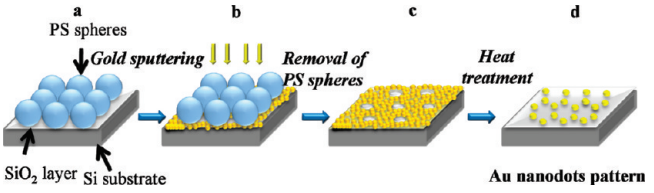


**Figure 1.** Schematic drawing of the realization of Au nanodot arrays using PS sphere patterns as a shadow mask for Au sputtering. Panels a−d show the different processing steps.

Au honeycomb mask to a hexagonal nanoparticle array has been reported with attention to the crystallinity, size, and shape of the Au particles.

## Experimental Section

Substrates were p-type (111) Si wafers (5−10 Ω cm) with a diameter of 4 in. Prior to patterning, the Si specimens were precleaned in acetone to remove any organic contaminants. The Si specimens, with native oxide layer, were then heated in air at 600 °C for 10 min to increase the thickness of the oxide layer to 5 nm. The substrate was then cleaned by a conventional RCA I process to obtain a hydrophilic surface, that is, a treatment with a 1:1:5 solution of $NH_4OH$ (25%), $H_2O_2$ (30%), and water at 80 °C for 15 min.[28] Hydrophilic surfaces were formed with terminal silanol (SiOH) groups.

After this pretreatment, a monodisperse suspension of polystyrene (PS) microspheres (Polysciences, Inc.) 1000 nm in diameter was spin-coated onto the substrate.[29] The suspension was dried in air at RT, and the spheres self-arranged into a close-packed structure of two-dimensional ordered lattices due to attractive capillary forces.[17]

In order to fabricate a Au thin-film pattern, the densely packed deposited PS spheres are used as a shadow mask. Au thin films were deposited onto the Si substrate through the PS honeycomb shadow mask using a Balzers SCD 040 sputter coater at a discharge current of 25 mA, voltage of 185V, and temperature of 25 °C in vacuum of 10 Pa for the desired time.

After sputtering, the PS mask was removed by immersing the specimens in 97% toluene using an ultrasonic bath. Finally, the specimens were annealed at several different temperatures for 1 h (heating rate 10 °C $min^{-1}$) in Ar atmosphere and then cooled to RT. This fabrication process is illustrated in Figure 1.

The Au patterns formed on the Si substrate were characterized by scanning electron microscopy (SEM, Hitachi S-4200, S-4800), EBSD (Genesis 4000 EDAX/TSL), atomic force microscopy (AFM), glow discharge optical emission spectroscopy (GDOES, JY RF-5000), and energy dispersive X-ray (EDX, Genesis 4000 EDAX).

## Results and Discussion

**Self-Organization of Polystyrene Spheres.** During NSL, a monolayer of PS spheres was created by controlling the sphere concentration and the spin coating parameters (time, speed, and cycles). The specimens were successfully coated with large domains of defect-free packing over the entire substrate surface (See Figure 2).

**Sputtering of Au into Thin Regular Honeycomb Patterns.** Thin layers of Au were deposited by sputtering through the PS shadow mask. The high mobility of the Au atoms during the sputtering process enabled the Au to cover the entire substrate surface even beneath the PS spheres except where the PS spheres actually contacted the Si substrates.[30] A honeycomb-like Au pattern, as shown in the SEM and AFM images in Figure 3a, resulted when the PS spheres were removed with toluene. These Au honeycomb-like patterns were subsequently annealed to study the mechanisms of transforming Au islands into Au NPs.

**Thermal Annealing of Au Pattern.** A sputtered-film thickness of 200 nm Au was used to study the dewetting

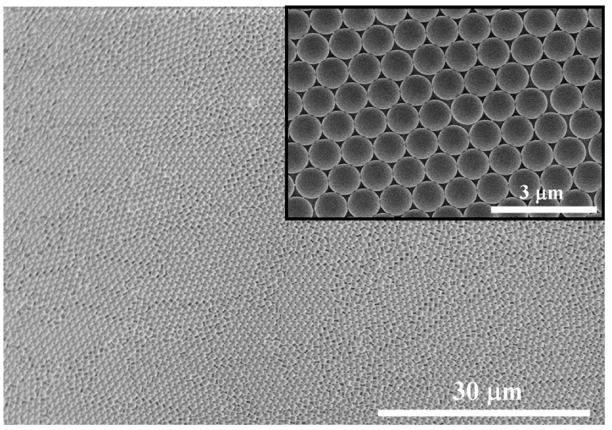


**Figure 2.** SEM images of a self-assembled monolayer of PS spheres with a diameter of 1 $\mu$m at different magnifications.

mechanism and self-organization into nanodots on Si substrates (thickness measured by a quartz crystal microbalance). After removing the PS spheres, the specimens were annealed in Ar for 1 h (heating rate 10 °C $min^{-1}$) at different temperatures, 400, 600, 800, and 1000 °C, and then cooled to RT. The well-aligned Au nanodot patterns formed on the Si substrate were analyzed by SEM and AFM and compared in Figure 3.

Traditionally, the term "sintering" refers to joining mechanisms between two particles or grains, usually within a bulk material, by mass transport. However, in the field of "catalyst science", the definition of word "sintering" is different. In this specific case, "sintering" is a process whereby clusters increase their size and reduce their number.[4] To avoid this confusion, we will use in this manuscript the term "thermal annealing" instead of "sintering". Two main mechanisms are well-known for this process: coalescence[4,31] and Ostwald ripening.[4,32]

Coalescence occurs when two nanoparticles are in contact and merge to form one larger nanoparticle. The driving force of this phenomenon is simply the natural tendency to reduce the total interfacial energy of the system. During particle coalescence, entire NPs can migrate on the substrate surface and coalesce if motion yields overall system-energy reduction. Nanodot coalescence results in a size distribution that is usually skewed toward larger particles.[31]

In contrast, Ostwald ripening occurs by removal (via evaporation or surface diffusion) of atoms from one nanoparticle and transfer to another one.[4,32] In this case, the particles are not in contact and the reduction of surface energy drives the mass transport. Both nanoparticles exchange atoms resulting in smaller nanoparticles losing atoms, and thereby becoming smaller, while the larger ones gain atoms and thus become even bigger. Nanodot Ostwald ripening results in a size distribution that is usually skewed toward smaller particles.

The Ostwald ripening process is the most common form of thermal annealing for metal nanoparticles well separated and supported on a surface, although coalescence can occur for a high density of clusters.[31,32] Plante et al.[32] recently pointed out that the self-assembly of Au islands/nanodots could possibly involve multiple and competitive mechanisms.

Thermal annealing processes involve then either migration of Au atoms (Ostwald ripening) or migration and coalescence of Au nanoparticles. As mentioned before, the

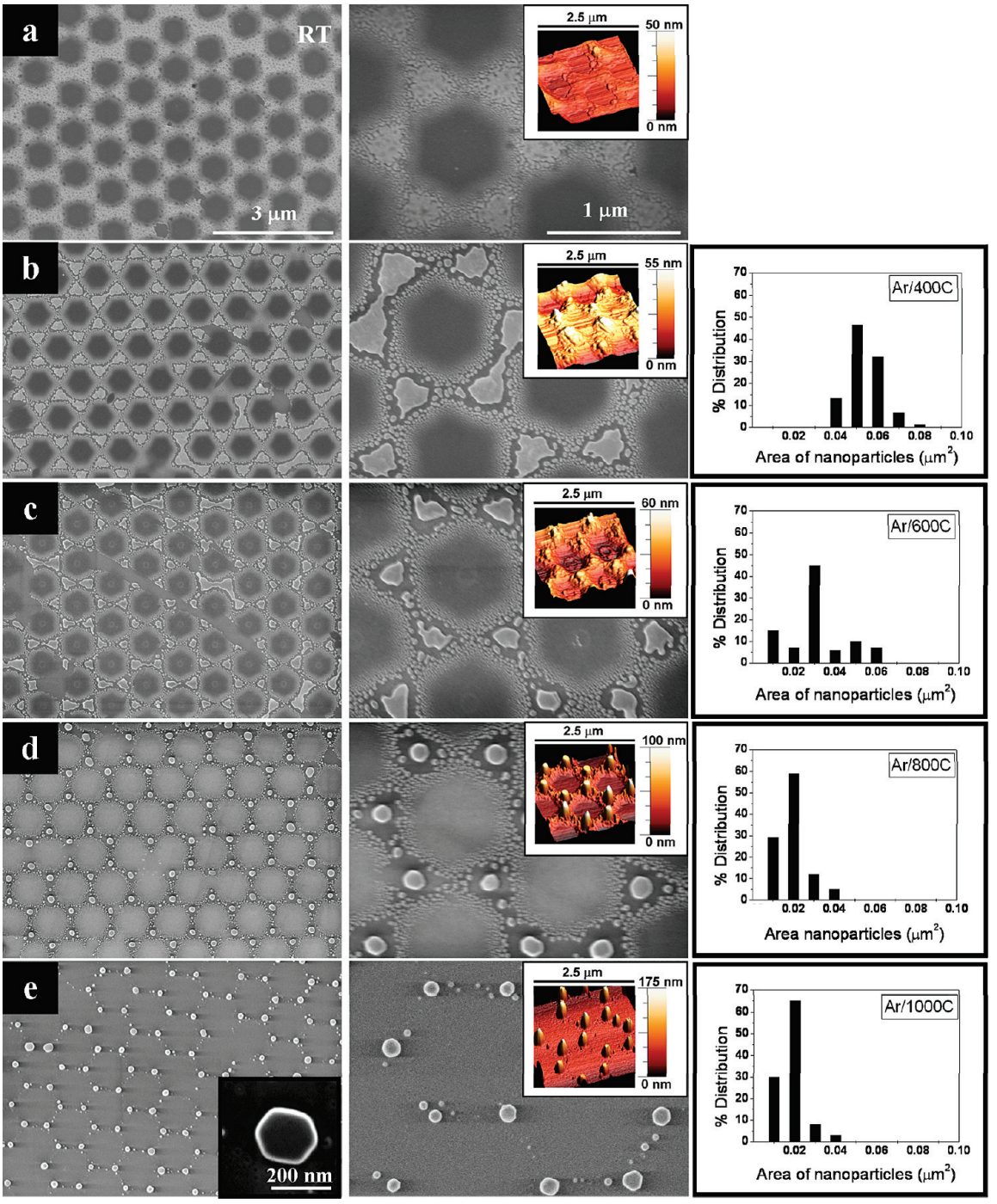


**Figure 3.** SEM and AFM images of a honeycomb Au mask prior to annealing (a) and SEM and AFM images of annealed Au island films on Si substrates in Ar for 1 h, and variation of the area distribution of Au nanoparticles depending on annealing temperature: (b) 400, (c) 600, (d) 800, and (e) 1000 °C.

thin Au film was deposited by sputtering. The high mobility of the Au atoms during the sputtering process resulted in Au covering all bare surface areas of the substrate, but the AFM image (Figure 3a) and the line scan at RT (Figure 4b) shows that the deposited Au layer thickness is slightly lower where the PS spheres shadow the substrate surface. We note here that the average height of Au layer thickness in non-shadowed areas is ~40 nm, while the deposited Au layer thickness is 200 nm. This finding is not well understood and could possibly be an artifact that occurs during PS sphere ultrasonic etching. In this processing step, part of the deposited Au film may be removed also. Peceros et al.[33] have shown that it is possible to decorate polystyrene microspheres with gold nanoparticles without prefunctionalizing their surfaces using the process of deposition−precipitation. The deposition of Au on PS spheres in addition to the $Si/SiO_2$ areas left visible by the hexagonal arrangement of PS spheres could be another reason for this finding. The Au island pattern is formed by an agglomeration of Au nanoparticles with diameters less than 3 nm.[34]

After heating at 400 °C, we conclude that the pattern formation will occur mainly by coalescence due to the high density of Au. The small nanoparticles will merge to form larger nanoparticles. After 1 h at 400 °C, SEM and AFM

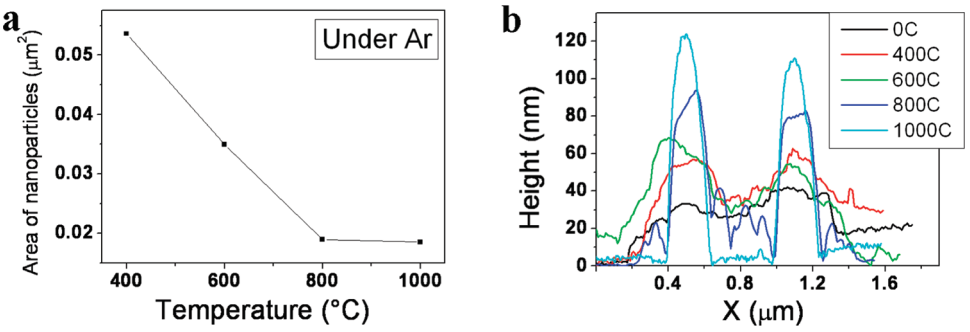


**Figure 4.** Variation of the Au nanodot area deduced from SEM images (a) and of the nanodot heights deduced from AFM measurements (b). All data have been taken after thermal annealing of Au island films on Si substrates in Ar for 1 h at various temperatures.

images (Figure 3b) and line scan (Figure 4b) show that the largest Au nanodots form in areas on the Si substrate where the thickest portions of the Au layer were deposited. In addition however, smaller Au nanoparticles, in the form of satellites to large center Au nanodots, occurred. The statistical analysis in the size distribution, taking into account only the large center Au nanodots, shows a profile skewed more toward larger particles, which would therefore suggest Au coalescence as the main mechanism for island formation.

At 600 °C, Au nanodot formation is a little different. Again, center Au nanodots form, but the area and number of satellite nanodots are smaller (cf. Figures 3c and 4b). The particle size distribution of the large center Au nanodots appears to be Gaussian. We assume that the formation of the Au nanodots at 600 °C could possibly involve both mechanisms (coalescence and Ostwald ripening) operating concurrently.

At 800 °C, the center Au nanodots are higher and smaller in footprint on the surface. Their size distribution (Figure 3d) shows a profile skewed more toward smaller particles, confirming that the Ostwald ripening mechanism is the dominant mechanism during thermal annealing of Au islands at this temperature. The large NPs grow at the expense of smaller NPs which shrink and eventually disappear. The shift in NP area distribution indicates that there is a change in pattern formation mechanism from coalescence to Ostwald ripening between 400 and 800 °C. Due to the high mobility of Au on Si surfaces, SMORS (surface-mediated Ostwald ripening sintering),[4] in which material is transferred from one nanoparticle to another by diffusion across the substrate surface, is more probable in this case.

At 1000 °C, the center Au nanodots stop decreasing in area but continue to increase their height. The size distribution (Figure 3e) shows a profile skewed more toward smaller particles, indicating again that the Ostwald ripening mechanism is the main mechanism. The AFM and SEM images (Figure 3e) show that all the satellite Au nanodots have disappeared and merged with the center Au nanodot. Thus, the Au island films have self-aligned in hexagonal Au nanodot arrays. The final Au nanodots have a diameter of ~100 nm, height of ~110 nm, and a spatial density of ~$3 \times 10^8$ $cm^{-2}$.

For the diffusion of Au in Si, it has been reported that at 1000 °C, one monolayer of pure Au on the surface is sufficient to saturate a 500 $\mu$m thick Si wafer.[35] It has been also reported that Au can diffuse through $SiO_2$ layers into the adjacent Si wafer.[36] Glow discharge optical emission spectroscopy (GDOES) measurements performed for our samples with patterned Au islands after thermal annealing at

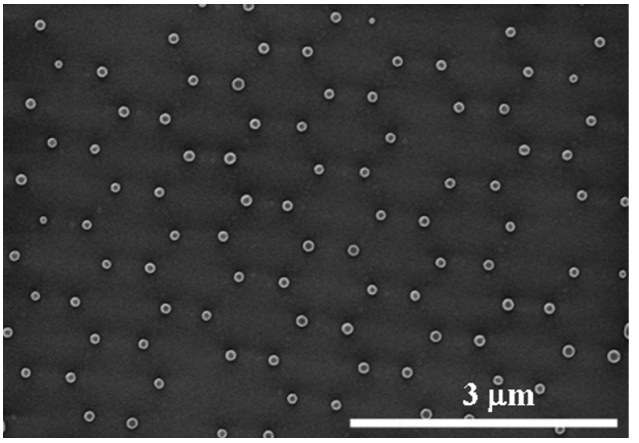


**Figure 5.** SEM image of Au nanodots: final annealing temperature 1000 °C for 2 h.

different temperatures (data is not shown here) do not show a significant influence of the patterning on the diffusion of Au in $SiO_2$ and Si.

As mentioned before, the Si substrate is heated in air at 600 °C for 10 min to increase the thickness of the oxide layer. GDOES measurements show that the Si oxide thickness is 5 nm. Since a porous alumina tube furnace was used for thermal annealing of the Au layers on Si, a small quantity of $O_2$ from the atmosphere can diffuse in the tube and results in formation of a $SiO_2$ layers even in the case of heating in Ar atmosphere, that is, intentionally oxide-free conditions. For this reason, we chose to have a thin layer of $SiO_2$ on our Si substrate right from the beginning of the experiment in order not to change the chemical surface composition during the experiment. The influence of the thickness of the $SiO_2$ layer on the Au nanodot formation and self-assembly was found to be marginal, that is, Au nanodot assemblies on nominally oxide-free Si (native oxide is most probably present) and on a relatively thick 100 nm $SiO_2$ layer on Si were essentially identical.

**Influence of the Thermal Annealing Time.** To study the influence of the thermal annealing time on the Au nanodot formation, the specimens have been prepared as described before. After sputtering 200 nm of Au films, the PS spheres were etched away, and thermal annealing in Ar for 2 h (heating rate 10 °C $min^{-1}$) at 1000 °C was carried out. As we showed before, at 1000 °C, Ostwald ripening is the main transport mechanism. SEM images (Figure 5) show that by increasing the thermal annealing time from 1 to 2 h, all the small satellite particles (nanodots) disappeared probably upon merging into the center nanodot. Therefore, doubling

the thermal annealing time at 1000 °C provides hexagonal arrays of Au nanodots without visible satellite nanodots between the center NPs. The diameters and thus the volumes of the Au nanodots in these patterns appear highly homogeneous from SEM data.

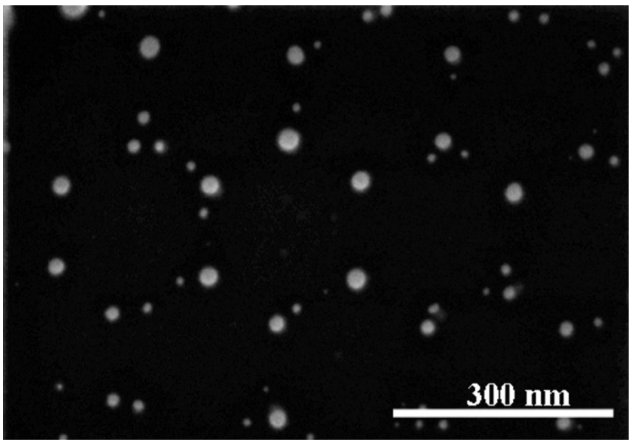


**Figure 6.** SEM image of annealed (final annealing temperature 800 °C) Au nanodot arrays. The mask patterning consisted of a monolayer of PS spheres with 200 nm diameters. The sputtered Au film was 140 nm thick.

**Influence of the Size of PS Spheres on Au Nanodot Array Formation.** The advantage of this PS sphere shadow mask patterning method is that it is simple and fast and the diameter and density of the PS spheres can be controlled to a certain extent so that certain pattern variations can be achieved. Figure 6 shows a Au nanodot array as a result of using PS spheres with diameters of 200 nm, versus 1000 nm, while using a 140 nm-thick Au film. The 140 nm thickness is set according to the experimental results that show that this is the optimal thickness at these conditions. The annealing temperature was 800 °C in Ar atmosphere for 1 h. The average diameter of the thermally treated nanodots is ~30 nm, and the spatial density is $\sim 5 \times 10^9$ cm$^{-2}$. By decreasing the size of PS spheres, we decrease the dimension of the Au nanodots and increase their density.

**Influence of Varied Au Film Thickness for Au Nanodot Array Formation.** We investigated the effect of varied sputtered Au film thicknesses on the size of the Au nanodots after thermal annealing. For that purpose, 20 nm (Figure 7a), 100 nm (Figure 7b), 200 nm (Figure 7c), and 300 nm (Figure 7d)

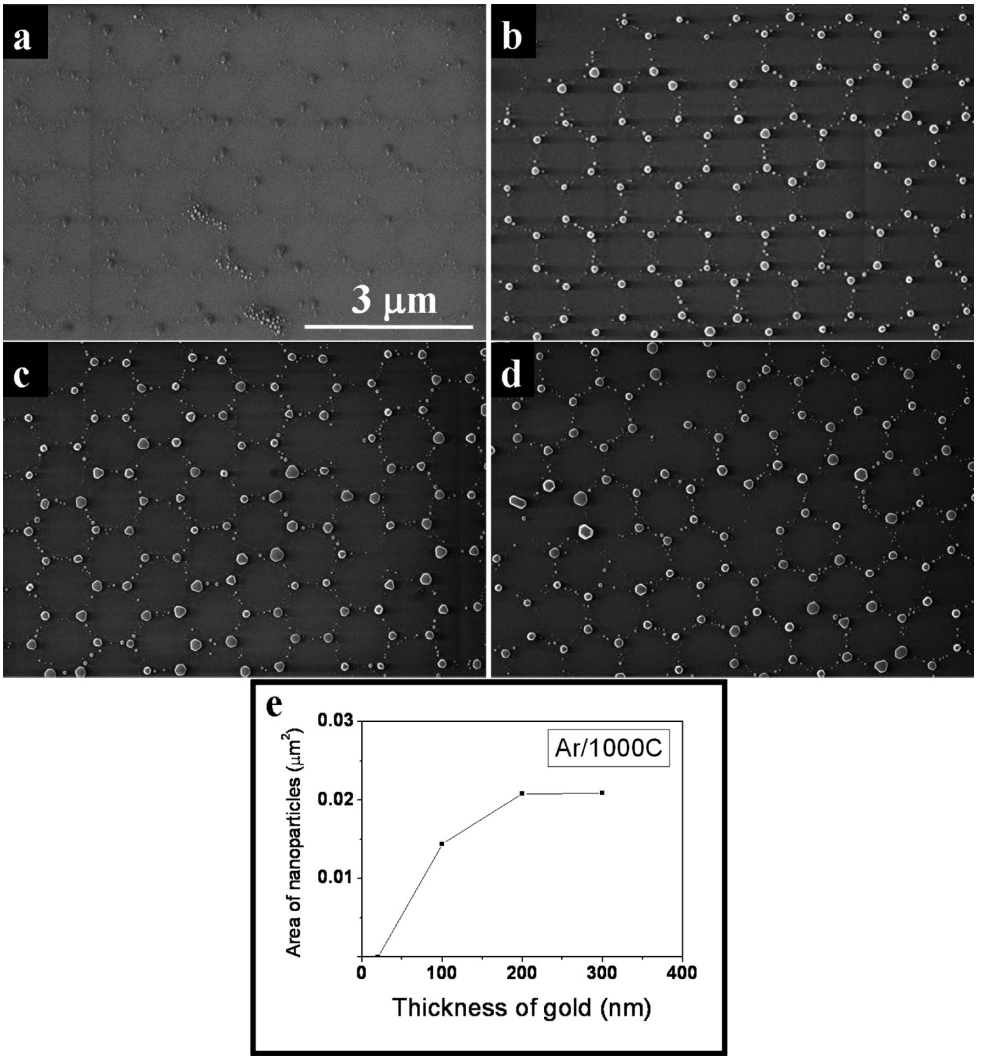


**Figure 7.** SEM images of hexagonal arrays of Au nanodots fabricated by annealing at 1000 °C in Ar atmosphere for 1 h. The diameter of the PS spheres was 1000 nm, and the thicknesses of the sputtered Au films varied: (a) 20 nm, (b) 100 nm, (c) 200 nm, and (d) 300 nm. Panel (e) shows the nanodot areas deduced from SEM data as a function of the thickness of the sputtered Au films measured by a quartz crystal microbalance.

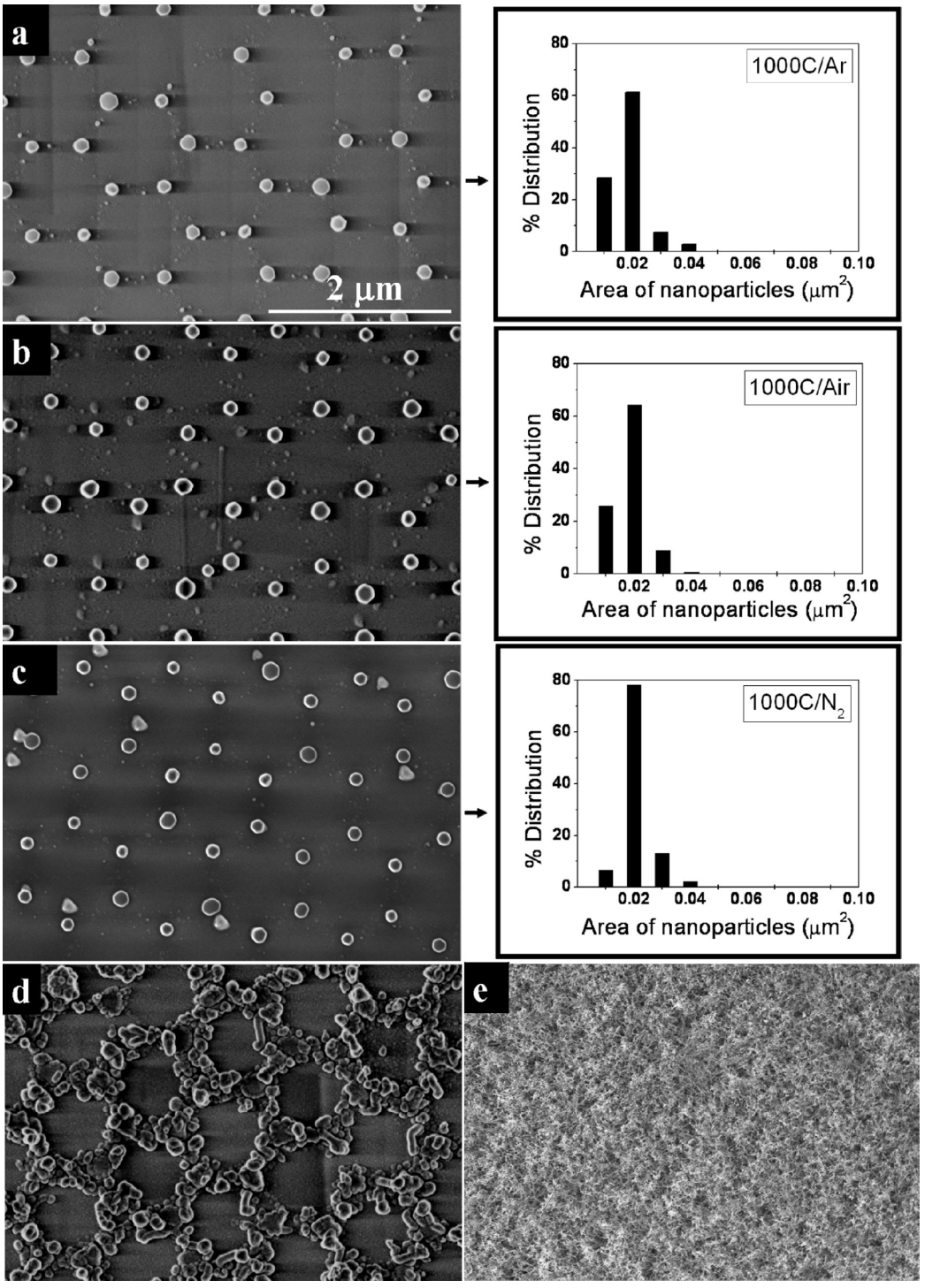


**Figure 8.** SEM images of Au nanodot arrays that formed after Au film sputtering (200 nm thick) through PS sphere shadow masks onto Si substrates and after annealing at 1000 °C for 1 h in different atmospheres: (a) Ar, (b) air, (c) $N_2$, (d) mixture of Ar and $H_2$, and (e) vacuum.

thick Au films were sputtered through the PS shadow masks onto the Si substrates. The Au thickness was measured by a quartz crystal microbalance. After etching away the PS spheres, the specimens were annealed in Ar for 1 h (heating rate 10 °C $min^{-1}$) at 1000 °C and were then cooled to RT. Figure 7a shows that, for a thin layer of Au (20 nm), the Au nanodots are very small without defined shapes. Figure 7b,c, e shows that when the thickness of the Au films is increased, the diameters (and volumes accordingly anticipating a half-spherical shape as suggested by AFM measurements) of the Au nanodots increase from ~100 nm (Figure 7b) to ~200 nm (Figure 7c). Figure 7d shows that when the thickness of the Au film is increased from 200 to 300 nm, the diameters of Au nanodots remain unchanged. As mentioned before, this finding is not well understood and is possibly an artifact that occurs during PS sphere ultrasonic etching. During this processing step, part of the deposited Au film may be removed too. The deposition of Au on PS spheres and not only on the $Si/SiO_2$ areas left visible by the hexagonal arrangement of PS spheres could be another reason for this finding.[33]

**Thermal Annealing Using Different Atmospheres.** The mobility of Au on the Si substrate is highly dependent on the annealing atmosphere. In order to study the pattern formation mechanism during thermal annealing in different atmospheres, 200 nm of Au was sputtered onto Si substrates through PS sphere shadow masks. After removal of the PS spheres, the specimens were annealed at 1000 °C for 1 h in different atmospheres: Ar (Figure 8a), air (Figure 8b), nitrogen (Figure 8c), a mixture of Ar and hydrogen (10%) (Figure 8d), and vacuum (Figure 8e). The major Au nanodot morphologies produced during thermal annealing of the sputtered Au film are the icosahedron ($I_h$), aka the "pancake", decahedron ($D_h$) identified as having a truncated triangular dipyramid (TTD) structure, and the fcc-truncated octahedron ($TO_h$). The specimens were characterized by SEM, EBSD, and EDX.

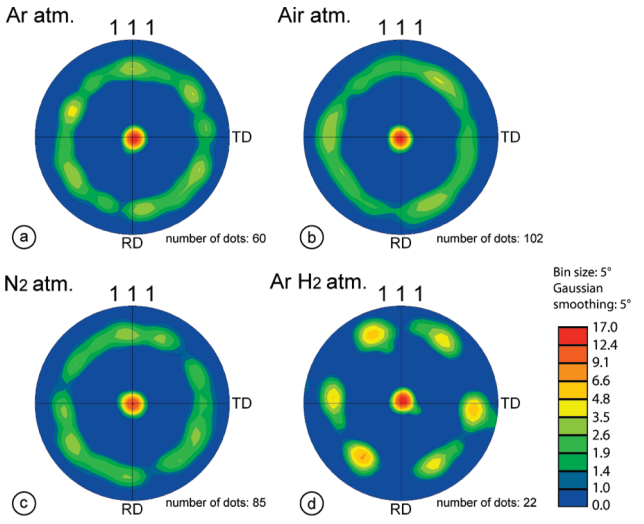


**Figure 9.** The ⟨111⟩ pole figures of the Au nanodots annealed in different atmospheres: (a) Ar, (b) air, (c) $N_2$, and (d) mixture of $Ar/H_2$.

**Thermal Annealing of Sputtered Au Islands on Si Substrates in Ar Atmosphere.** Figure 8a shows an SEM image of a specimen with the aforementioned parameters annealed at 1000 °C in Ar. The size distribution of Au nanodots is similar to the one shown in Figure 3e. In this case, the morphology of the organized Au nanodots is fcc-truncated octahedral ($TO_h$) (Figure 3e). This result seems to coincide well with the simulations of Grochola et al.,[37] who demonstrate that fcc-based morphologies are more likely to form in large NP populations. We note here that our Au nanodots have a size of ~100 nm in diameter. EBSD analyses have been carried out in order to measure the orientations of the Au nanodots and their single crystallinity; 60 Au nanodots have been analyzed. The results give a clear ⟨111⟩ fiber texture of the Au nanodots annealed in Ar atmosphere (Figures 9a and 10a). Detailed EBSD maps on a single dot show that they are in general monocrystalline (Figure 10b). In a few cases, a first-order twin boundary (Σ3, 60° rotation around ⟨111⟩) is observed inside the dot (Figure 10c).

**Thermal Annealing of Sputtered Au Islands on Si Substrates in Air.** Figure 8b shows an SEM image of a specimen with the aforementioned parameters annealed at 1000 °C in air. The statistical analysis of the size distribution of the Au nanodots shows a profile skewed more toward smaller particles, which would therefore suggest that the Ostwald ripening mechanism is again the dominant mechanism during thermal annealing in air atmosphere. Again, the morphology of obtained Au nanodots is fcc-truncated octahedrons ($TO_h$), and the diameter is also around 100 nm. This result shows that annealing in air does not have an impact on the morphology and the size of the Au nanoparticles. We note here that EDX and GDOES measurements show an increasing thickness to around 80 nm of the $SiO_2$ layer. This result shows again that the thickness of the $SiO_2$ layer does not have an impact on the organization, morphology, and size of the Au nanodots. EBSD analyses on 102 Au nanodots (Figure 9b) show a ⟨111⟩ fiber texture of the Au nanodots similar to the sample annealed in Ar. This result demon-

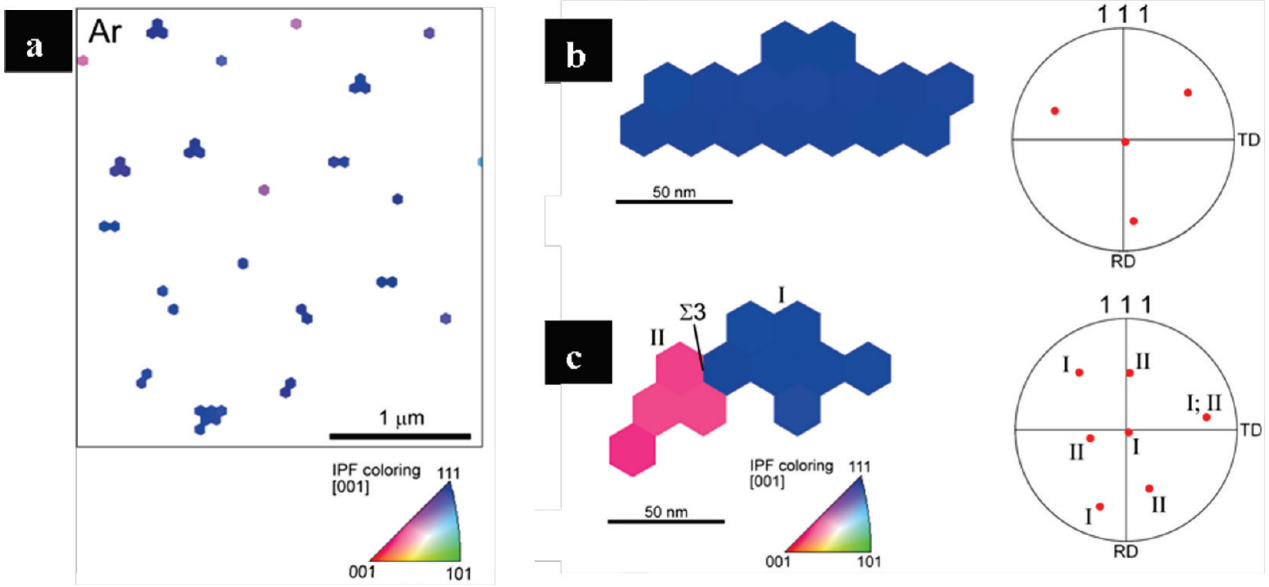


**Figure 10.** (a) EBSD maps (75 nm step size) of the Au nanodots in the sample annealed in Ar atmosphere. Only those points are shown in the maps that have a high confidence index (> 0.1). The hexagonal array arrangement of the Au nanodots is well recognized. Most of the dots have a ⟨111⟩ axis normal to the Si(111) substrate surface. (b, c) Detailed EBSD maps (20 nm step size) showing a monocrystalline Au nanodot with a ⟨111⟩ surface normal orientation and a nanodot with a Σ3 twin boundary, respectively.

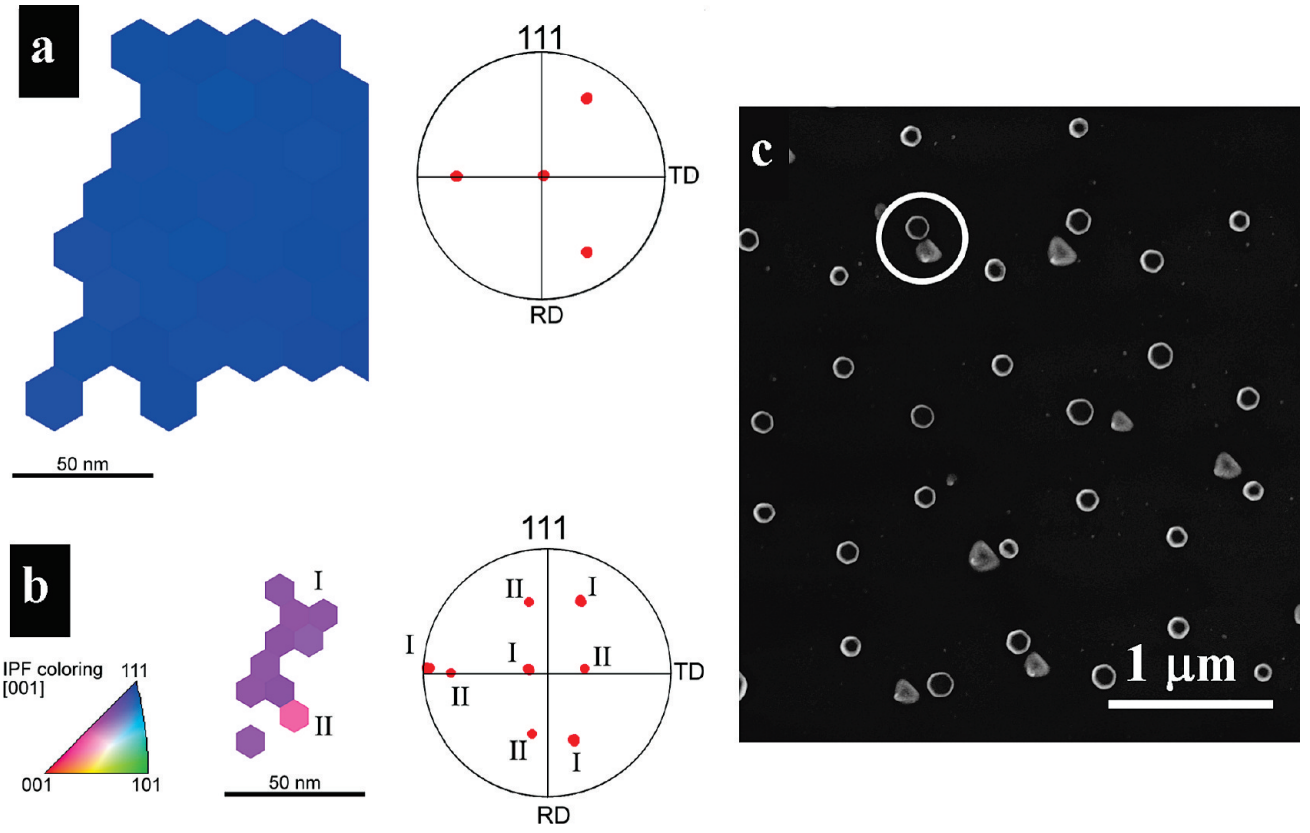


**Figure 11.** (a) EBSD map (20 nm step size) of a Au nanodot annealed in $N_2$ atmosphere showing a ⟨111⟩ orientation. (b) EBSD map (10 nm step size) of a small satellite Au nanodot close to the center nanodot forming the hexagonal lattice. Its orientation is a few degrees off the orientation of the center dot (cf. points I in the pole figure). The indexed point II in the pole figure has an orientation not far from a Σ3 twin relation with respect to point I. (c) SEM image of the annealed sample with Au nanodot pattern. The circle indicates the two dots on which the shown EBSD patterns have been measured.

strates that annealing in air does not play a significant role for the orientation of Au nanodots.

**Thermal Annealing of Sputtered Au Islands on Si Substrates in $N_2$.** Figure 8c shows an SEM image of a specimen with the aforementioned parameters annealed at 1000 °C in $N_2$. In this case, the particle size distribution appears to be Gaussian. We assume that the self-assembly of the Au nanodots involves the two mechanisms (coalescence and Ostwald ripening) competitively. The diameter of these NPs is similar to the ones having around 100 nm diameters from previous processes. In this case, two different shapes of nanoparticles have been observed: the nanoprism identified as having a truncated triangular dipyramid (TTD) structure, and the fcc-truncated octahedron ($TO_h$). Grochola et al.[37] demonstrated that the coalescence mechanism results in a dominant occurrence of truncated triangular dipyramid (TTD). A thermodynamic interaction between Au atoms and $N_2$ molecules could be the reason for the change in the mechanism, but more experiments and simulations are necessary to better understand these phenomena. EBSD analyses on 85 Au nanodots show a ⟨111⟩ fiber texture of the Au nanodots similar to the samples annealed in the other atmospheres (Figure 9c). Figure 11a shows a detailed EBSD map of the fcc-truncated octahedral ($TO_h$) Au nanodot annealed in $N_2$. The dot is monocrystalline. Figure 11b shows an EBSD map of the truncated triangular dipyramid (TTD) Au dot. Its orientation is very similar to the dot in Figure 11a, slightly off the ⟨111⟩ orientation by a few degrees. This dot is monocrystalline except for a Σ3 twin boundary. In summary, the TTD nanodots are those that can be found between the center nanodots well arranged in a hexagonal lattice. These satellite nanodots often show a slight misorientation between neighboring nanodots and the center dots. Some of them show twin boundaries that disturb single crystallinity. We assume that the formation of these nanodots is due to the concurrence of the two mechanisms (coalescence and Ostwald ripening) when annealing at 1000 °C in $N_2$. This result proves that the mechanism of pattern formation plays a main role on the shape and the orientation development of Au nanodots.

**Thermal Annealing of Sputtered Au Islands on Si Substrates in Ar and $H_2$ Atmosphere.** In the mixture of Ar and $H_2$ (reducing atmosphere) and after heat treatment at 1000 °C, we do not observe the formation of a pattern of nanodots as before (Figure 8d). This suggests that thermal annealing in a reducing atmosphere ($H_2$-ambient) inhibits the Ostwald ripening mechanism and the pattern formation of Au occurs only by coalescence. The small NPs will merge to form larger NPs, but the shape of the honeycomb mask will still be conserved. EDX measurement performed during SEM observations allows for studying locally the chemical composition of Au patterns without any influence of the substrate. We note here that in this case, the spatial resolution of EDX for an accelerating voltage of 6 kV estimated by the parametrized Kanaya−Okayama electron range ($R_E$) is 55 nm.[38] The spatial resolution is smaller than the nanodots' size (~100 nm). This measurement does not show any significant difference between the chemical composition of

specimens annealed in $H_2$, inert atmospheres (Ar, $N_2$), or oxidizing (air) atmospheres. Such behaviors could possibly be due to varied surface properties at high temperatures. The results can be discussed and interpreted in terms of metal−oxygen bonding at the metal−$SiO_2$ interfaces. Thus, the number of metal−oxygen bonds (per unit area) at substrate surfaces annealed in reducing atmosphere ($H_2$) should be less than the number of metal−oxygen bonds at substrate surfaces annealed in oxidizing (air) atmosphere or inert (Ar, $N_2$) atmosphere.[39] Plante et al. have already shown that the surface compositions play a dominant role in the self-assembly of Au nanodots during thermal annealing.[32] Miotello et al.[40] showed that annealing in an oxidizing atmosphere (air) favors the Ostwald ripening mechanism at high temperature compared with an inert atmosphere. They correlate this to a thermodynamic interaction between Au atoms and $O_2$ molecules. The decreasing number of metal−oxygen bonds or the thermodynamic interaction between Au atoms and $O_2$ molecules could be the reason for reduced or hindered migration of Au atoms and the pattern formation by Ostwald ripening when annealing in reducing atmosphere. EBSD analyses on 22 Au nanodots again show a ⟨111⟩ orientation of the Au nanodots (Figure 9d). The pole figure in Figure 9d shows two preferentially different ⟨111⟩ orientations. This is due to the limited number of well-indexed points (64 versus more than 120 points in the other samples) mainly due to a strong surface roughness created by the juxtaposing nanodots (Figure 8d). Strong surface roughness leads to a shadowing of the backscattered electrons. Individual Au particle measurements on this sample show that particles also tend to have a random ⟨111⟩ fiber texture.

**Thermal Annealing of Sputtered Au Islands on Si Substrates in Vacuum.** SEM characterizations of samples annealed in vacuum at 800 °C show that the morphology of Au nanodots is similar to that observed after annealing in Ar at 800 °C (Figure 3d). Therefore annealing in vacuum up to 800 °C does not have a significant influence on the mechanism of the formation of nanodots or migration of Au on the Si surface. But at 1000 °C (Figure 8e), we observed the formation of a forest of nanowires. EDX characterization shows that these nanowires are composed of oxidized silicon. The formation mechanism of the nanowires can be OAG (oxide-assisted growth) with Au catalyst similar to the ones observed by Yao et al.[41] for the growth of Si nanowires. The reaction between the Si and the oxide layer will lead to the formation of $SiO_x$. This reaction is accelerated by the vacuum ambient. This can be the reason why the growth of nanowires occurs only in vacuum and not in atmospheric pressure. As the $SiO_x$ vapor arrives at the Au nanodots, $SiO_x$ will dissociate at the particle surface into Si and $SiO_2$. Si will dissolve in the Au nanodot to form the eutectic Au−Si alloy, while the Si oxide will remain at the particle surface. When the Si concentration in the Au particle reaches supersaturation, Si will separate out at the interface and grow on the Si substrate. Si oxide will flow over the Au particle surface and form a layer covering the nanowires. Exposure to small amounts of oxygen present in the furnace oxidizes the nanowires immediately after formation. More experiments are in progress in order to study the influence of different parameters (temperature, time, thickness of gold and silica layer, etc.) and to better understand the growth mechanism of these $SiO_2$ nanowires.

## Conclusion

In summary, the synthesis of well-organized arrays of Au NPs has been studied. We show the transformation mechanism of a Au film to a hexagonal array of Au NPs by thermal annealing at different temperatures and in different atmospheres. We demonstrated that the mechanism of pattern formation can be coalescence, Ostwald ripening or a combination of the two and varies as a function of temperature and the annealing atmosphere. The controllability of the organization, morphology, and crystallinity by EBSD has been studied. The results prove that the annealing atmosphere does not play a significant role in the orientation of Au nanodots. The formation of fcc-truncated octahedrons ($TO_h$) is observed in Ar and air, while the truncated triangular dipyramid (TTD) morphology is observed in $N_2$. In $H_2$, we do not observe Au nanodot formation upon thermal annealing because the Ostwald ripening mechanism is totally inhibited, and in vacuum we observe the formation of $SiO_2$ nanowires. This study opens the way to better control of the mechanism of the thermal annealing of different supported metals as a function of the chemical composition of the supported surface, the temperature, and the atmosphere. This is a key point for the use of organized metallic NPs for growth of 1D nanostructures, for chemical catalysis, or as plasmonic structures.

**Acknowledgment.** Financial support by the European Commission in the FP7 framework is acknowledged (HYDROMEL and ROD_SOL). We gratefully thank Laurent Bernau and Roland Widmer for AFM measurements, William Mook for scientific discussion, and Max Aeberhard for GDOES measurement.

## References

(1) Daniel, M. C.; Astruc, D. *Chem. Rev.* **2004**, *104* (1), 293–346.
(2) Gai, Z.; Howe, J. Y.; Guo, J. D.; Blom, D. A.; Plummer, E. W.; Shen, J. *Appl. Phys. Lett.* **2005**, *86*, No. 023107.
(3) Albrecht, M.; Hu, G.; Guhr, I. L.; Ulbrich, T. C.; Boneberg, J.; Leiderer, P.; Schatz, G. *Nat. Mater.* **2005**, *4* (3), 203–206.
(4) Bowker, M. *Nat. Mater.* **2002**, *1* (4), 205–206.
(5) Xu, W. L.; Zheng, M. J.; Ding, G. Q.; Shen, W. Z. *Chem. Phys. Lett.* **2005**, *411* (1−3), 37–42.
(6) Sato, K.; Hosokawa, K.; Maeda, M. *J. Am. Chem. Soc.* **2003**, *125* (27), 8102–8103.
(7) Maxwell, D. J.; Taylor, J. R.; Nie, S. *J. Am. Chem. Soc.* **2002**, *124* (32), 9606–9612.
(8) Ross, F. M.; Tersoff, J.; Reuter, M. C. *Phys. Rev. Lett.* **2005**, *95*, No. 146104.
(9) Dailey, J. W.; Taraci, J.; Clement, T.; Smith, D. J.; Drucker, J.; Picraux, S. T. *J. Appl. Phys.* **2004**, *96*, 7556–7567.
(10) Buckmaster, R.; Hanada, T.; Kawazoe, Y.; Cho, M. W.; Yao, T.; Urushihara, N.; Yamamoto, A. *Nano Lett.* **2005**, *5* (4), 771–776.
(11) Stodolka, J.; Nau, D.; Frommberger, M.; Zanke, C.; Giessen, H.; Quandt, E. *Microelectron. Eng.* **2005**, *78*−*79*, 442–447.
(12) Chun, Y. J.; Nakajima, S.; Kawabe, M. *Jpn. J. Appl. Phys.* **1996**, *35*, L1075–L1076.
(13) DenBaars, S. P.; Reaves, C. M.; Hill, V. B.; Varma, S.; Weinberg, W. H.; Petroff, P. M. *J. Cryst. Growth* **1994**, *145* (1−4), 721–727.
(14) Wang, L.; Montagne, F.; Hoffmann, P.; Pugin, R. *Chem. Commun.* **2009**, 3798–3800.
(15) Santhanam, V.; Liu, J.; Agarwal, R.; Andres, R. P. *Langmuir* **2003**, *19*, 7881–7887.
(16) Masuda, H.; Yasui, K.; Nishio, K. *Adv. Mater.* **2000**, *12* (14), 1031–1033.
(17) Deckman, H. W.; Dunsmuir, J. H. *Appl. Phys. Lett.* **1982**, *41*, 377–379.
(18) Huang, Z.; Fang, H.; Zhu, J. *Adv. Mater.* **2007**, *19* (5), 744–748.
(19) Ma, W.; Hesse, D.; Gösele, U. *Nanotechnology* **2006**, *17*, 2536–2541.

(20) Asoh, H.; Arai, F.; Ono, S. *Electrochem. Commun.* **2007**, *9* (4), 535–539.
(21) Shen, H.; Cheng, B.; Lu, G.; Ning, T.; Guan, D.; Zhou, Y.; Chen, Z. *Nanotechnology* **2006**, *17*, 4274–4277.
(22) Haes, A. J.; Zou, S.; Schatz, G. C.; Van Duyne, R. P. *J. Phys. Chem. B* **2004**, *108*, 6961–6968.
(23) Burmeister, F.; Badowsky, W.; Braun, T.; Wieprich, S.; Boneberg, J.; Leiderer, P. *Appl. Surf. Sci.* **1999**, *144−145*, 461–466.
(24) Sun, F.; Cai, W.; Li, Y.; Duan, G.; Nichols, W. T.; Liang, C.; Koshizaki, N.; Fang, Q.; Boyd, I. W. *Appl. Phys. B: Laser Opt.* **2005**, *81*, 765–768.
(25) Tan, B. J. Y.; Sow, C. H.; Koh, T. S.; Chin, K. C.; Wee, A. T. S.; Ong, C. K. *J. Phys. Chem. B* **2005**, *109* (22), 11100–11109.
(26) Müller, C. M.; Mornaghini, F. C. F.; Spolenak, R. *Nanotech.* **2008**, *19*, No. 485306.
(27) Sakamoto, S.; Philippe, L.; Bechelany, M.; Michler, J.; Asoh, H.; Ono, S. *Nanotech.* **2008**, *19*, No. 405304.
(28) Fuhrmann, B.; Leipner, H. S.; Höche, H.-R.; Schubert, L.; Werner, P.; Gösele, U. *Nano Lett.* **2005**, *5* (12), 2524–2527.
(29) Bechelany, M.; Brodard, P.; Philippe, L.; Michler, J. *Nanotechnology* **2009**, *20*, No. 455302.
(30) Wang, X.; Summers, C. J.; Wang, Z. L. *Nano Lett.* **2004**, *4* (3), 423–426.
(31) Datye, A. K.; Xu, Q.; Kharas, K. C.; McCarty, J. M. *Catal. Today* **2006**, *111* (1−2), 59–67.
(32) Plante, M. C.; Garrett, J.; Ghosh, S. C.; Kruse, P.; Schriemer, H.; Hall, T.; LaPierre, R. R. *Appl. Surf. Sci.* **2006**, *253* (4), 2348–2354.
(33) Peceros, K. E.; Xu, X. D.; Bulcock, S. R.; Cortie, M. B. *J. Phys. Chem. B* **2005**, *109* (46), 21516–21520.
(34) Satpati, B.; Goswami, D. K.; Roy, S.; Som, T.; Dev, B. N.; Satyam, P. V. *Nucl. Instrum. Methods Phys. Res., Sect. B* **2003**, *212*, 332–338.
(35) Mathiot, D. *Phys. Rev. B* **1992**, *45*, 13345–13355.
(36) Schmidt, P. F.; Adda, L. P. *J. Appl. Phys.* **1974**, *45*, 1826–1833.
(37) Grochola, G.; Russo, S. P.; Snook, I. K. *J. Chem. Phys.* **2007**, *126*, No. 164707.
(38) Utke, I.; Hoffmann, P.; Melngaillis, J. *J. Vac. Sci. Technol., B* **2008**, *26* (4), 1197–1276.
(39) Li, J. G.; Gao, J. *Mater. Lett.* **2006**, *60*, 1323–1326.
(40) Miotello, A.; De Marchi, G.; Mattei, G.; Mazzoldi, P.; Sada, C. *Phys. Rev. B* **2001**, *63*, No. 075409.
(41) Yao, Y.; Li, F.; Lee, S.-T. *Chem. Phys. Lett.* **2005**, *406*, 381–385.